Review of Scientific Instruments

RESEARCH ARTICLE | FEBRUARY 01 2023

Development of a three-degree-of-freedom piezoelectric actuator

Fenglong Wei ; Xueliang Wang; Jingshi Dong; Kang Guo; Yongxin Sui

Rev. Sci. Instrum. 94, 025001 (2023)
https://doi.org/10.1063/5.0114030

AIP Publishing

Review of Scientific Instruments ARTICLE scitation.org/journal/rsi

Development of a three-degree-of-freedom piezoelectric actuator

Cite as: Rev. Sci. Instrum. 94, 025001 (2023); doi: 10.1063/5.0114030
Submitted: 25 July 2022 • Accepted: 7 January 2023 •
Published Online: 1 February 2023

Fenglong Wei,[1,2,a)] Xueliang Wang,[1,2] Jingshi Dong,[3] Kang Guo,[1,2] and Yongxin Sui[1,2]

AFFILIATIONS

[1] Changchun Institute of Optics, Fine Mechanics and Physics, Chinese Academy of Sciences, Changchun 130033, China
[2] University of Chinese Academy of Sciences, Beijing 100049, China
[3] School of Mechanical and Aerospace Engineering, Jilin University, Changchun 130025, China

[a)] **Author to whom correspondence should be addressed:** weifenglong@cnepo.com.cn

ABSTRACT

Multi-degree of freedom piezoelectric actuators are strongly needed for industrial applications, especially when manipulating a large and heavy mirror or lens in an optical system. A novel three-degree-of-freedom piezoelectric actuator, which is driven by two pairs of piezo-stack actuator with spatial compliant mechanisms designed to guide the motion and preload the piezo-stack actuators, is herein proposed. The structure and working principle of the proposed actuator are illustrated and its kinematic characteristic is analyzed. The stiffness of the spatial compliant mechanisms is modeled, and the dynamic characteristics are analyzed, Finite Element method is utilized to validate the correctness of the stiffness modeling and the free vibration analysis of the proposed actuator. A prototype actuator is fabricated and its output performances have been tested. Working space of X ranging from −7.1 to 5.6 μm, Y ranging from −6.2 to 8.2 μm and Z ranging from −2.3 to 2.1 μm, displacement resolutions of 15/16/21 nm along X-/Y-/Z-axis and average velocities of 52.3, 82.8 and 29.5 μm/s along X-axis, Y-axis, and Z-axis with carrying load up to 2 kg and driving frequency of 500 Hz have been achieved by the prototype actuator. The method of waveform generating for the proposed actuator has been developed with the inverse hysteresis compensation, and test results indicate that the positioning accuracy of the prototype actuator in the open loop has been improved from 0.94 to 0.23 μm for a circular trajectory tracking, from 0.48 to 0.29 μmm for an elliptical trajectory tracking, and from 0.61 to 0.32 μm for a rectangular trajectory tracking with the compensated waveform of driving voltage.

I. INTRODUCTION

Piezoelectric actuators, with advantages of high accuracy, fast response, and high stiffness, are widely used in scientific research and industrial applications, such as precision manufacturing[1–4] and metrology,[5,6] precision positioning[7–9] and scanning, microscopic,[10–12] lithography devices, and semiconductor processes.[13–17]

According to design and functionality, the piezoelectric actuators are classified as traditional actuators, piezoelectric stepping actuators, and multi-degree of freedom actuators.[18] The traditional actuators are usually referred to as simple piezo-driving components, including piezo-patch actuators, piezo-stack actuators, piezo-tube actuators, and piezo-amplified actuators, most of which have already been commercialized and can be easily bought in the market with small working range, simple construction, low driving, and controlling cost. For example, many different types of piezo-stack actuators working in longitudinal mode or shearing mode have been used as the driving components in lots of inchworm-type linear and rotary motors in papers,[19–26] with only one degree of elongating or shearing freedom, the piezo-stack actuators can push a shaft or a mover forward or backward with simple driving signals. The piezoelectric stepping actuators, usually referred to as highly integrated piezoelectric motors, have been developed mainly for a large range of precision motion with different operating modes[15] and they usually utilize traditional actuators as the core-driving source. As commercialized piezoelectric motors using the clamping and feeding actuation mode,[27] the PiezoWalk Actuators[28] have been developed by Physik Instrumente and Piezo LEG Actuators[29] have been developed by PiezoMotor, these two highly integrated bidirectional piezoelectric motors can continuously move with long working range and high resolution, making them widely used in Lithography and Semiconductor technology.[30,31]

With the requirements of large stroke multi-degree motion with high accuracy, multi-degree of freedom (MDOF) piezoelectric actuators are strongly needed for industrial applications. Multi-degree of freedom motion can be usually achieved through serial or parallel configuration of the traditional piezoelectric actuators or the piezoelectric stepping actuator or both.[32–34] A lot of commercialized products and research have been conducted on the realization of multi-degree motion of piezoelectric actuators for different specific applications[35–38] and many MODF piezoelectric actuators have been developed but with little consideration of high accuracy, high-carrying capability, high stiffness, and compact size along with multi-degree of freedom motion at the same time. For example, PI has developed an MDOF piezoelectric actuator (PICA P-153) with three translational motions[28] through the serial configuration of multiple piezo-stack actuators working in a longitudinal and shearing mode, which shows the perfect performance of compact size and high accuracy, but has relatively low transversal stiffness and is very easy to break when working with transversal static or inertial force. Piezoelectric actuator products have been developed with translational and rotational motions to actuate a fast steering mirror with high resolution,[28,39] but these products do show not enough high-carrying capability and can only manipulate mirrors with relative small diameter and less weight. Particularly when manipulating a larger and heavier lens/mirror in a Lithographic projection lens or a Three-Mirror off axis optical system, multiple MDOF piezoelectric actuators with high accuracy, high-carrying capability, high longitudinal and transversal stiffness, and compact size are needed to actuate the Movable part through the friction Contact Points in a design configuration as shown in Fig. 1, using the clamping and feeding actuation mode, a lens/mirror can then be manipulated with large working range and high positioning accuracy to move along with the Movable part in plane XY.

Thus, in this paper, an MDOF piezoelectric actuator with three degrees of freedom, has been designed, analyzed, fabricated, and tested. The emphasis of this paper is focused firstly on the structural design and analysis to realize MDOF motions, high stiffness, high-carrying capability, and compact size and secondly on the investigation of the method to improve its trajectory tracking performance. The paper is organized as follows: the structure of the three-degree-of-freedom piezoelectric actuator is designed and its kinematic characteristics are analyzed in Sec. II. The stiffness of the proposed actuator is modeled, and the dynamic characteristics of the proposed actuator are analyzed in Sec. III. The output performances and trajectory tracking performances of the prototype actuator are tested and evaluated in Sec. IV. The conclusions are given in Sec. V.

II. STRUCTURAL DESIGN AND KINEMATIC ANALYSIS

The structure and working principle of the three-degree-of-freedom piezoelectric actuator are shown in Fig. 2. Two pairs of piezo-stack actuators abbreviated to PA1 ~PA4 in Figs. 2(a) and 2(b) are parallelly aligned along X and Y axes with the same distance to the center axis and actuated separately to drive the Mover. Aluminium-oxide balls are bonded to the top of the piezo-stack actuators to provide a single contact point between the Mover and PA1/PA2/PA3/PA4. The four piezo-stack actuators are bonded to the stator at the bottom and pre-loaded by multiple Belleville Springs (SRBN5.2, MISUMI, JAPAN) through the flexible rod and the Mover to improve its dynamic operating performance.

The outer ring of an annular plate is fixed to the stator by Plate mountings, and the inner ring of the annular plate is fixed to the Mover by the flexible rod. The annular plate and the flexible rod are parallelly connected to guide the Mover to translate in z direction, with which guidance the Mover can also rotate around ox/oy axes. The end-effector contacting directly with the Movable Part at the Contact Point (CP) as shown in Fig. 1 is mounted on the Mover and can translate and rotate along with the Mover, the CP will translate along Z-axis while the Mover moves in z direction and will translate along X-/Y-axis when the Mover rotates around ox/oy axes, which indicates that the proposed actuator has three translational degrees of freedom.

The proposed actuator has the following advantages with the above structural design configuration: (a) Four piezo-stack actuators are designed parallelly to drive the end-effector, which serves as a friction element at the Contact Point to move with three totally

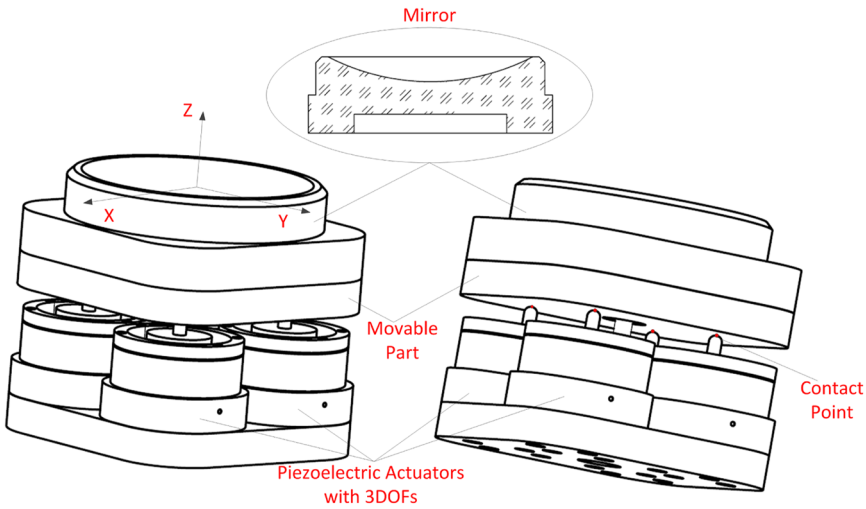

FIG. 1. Configuration of manipulating a large and heavy mirror.

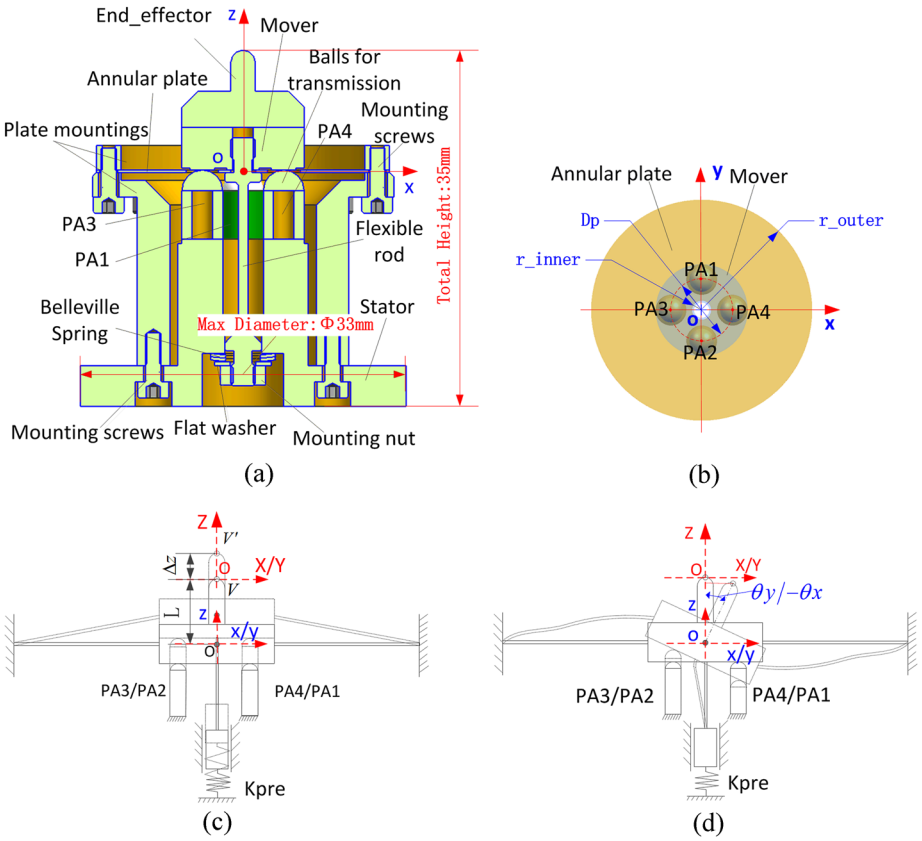

FIG. 2. Configuration of the three-degree-of-freedom piezoelectric Actuator. (a) Front cross-section view. (b) Top view. (c) Schematic diagram of translation along z-axis. (d) Schematic diagram of rotation around x-axis/y-axis.

decoupled translational degrees of freedom. (b) An annular plate firstly parallelly connecting with a flexible rod in space and then serially connecting with several commercialized Belleville Springs are designed to guide the motion and preload the piezo-stack actuators, the preload force can be adjusted through screwing or unscrewing the Mounting nut to balance with the carrying load, which can improve the carrying capability of the proposed actuator. (c) High longitudinal stiffness has been achieved through the parallel configuration of four piezo-stack actuators and high transversal stiffness has been ensured by the large radial stiffness of the annular plate. (d) The proposed actuator has a compact size and any piezo-stack actuator with an outer diameter of less than 6 mm and total length less than 20 mm can be packaged within this structure configuration without changing the outline size (ϕ33 mm × 35 mm) of the proposed actuator, and the longer the piezo-stack actuators are packaged within, the larger working ranges can be achieved.

To simplify the kinematic analysis, the three-degree-of-freedom actuator is simplified to the model illustrated in Figs. 1(c) and 1(d). For a piezo-stack actuator, the relationship between its output displacement and input driving voltage without considering hysteresis and creep effects is listed[18,40] as follows:

$$\begin{cases} \delta z_i(t) = n\Delta l d_{33} U_i(t) \\ 0 \le U_i(t) \le U_{\max} \\ i = 1,2,3,4, \end{cases} \tag{1}$$

where $\delta z_i(t)$ and $U_i(t)$ are the output displacement and input driving voltage of PA_i, $U_{\max}$ is the maximum driving voltage for piezo-stack piezoelectric actuator, Δl is the thickness of one piezo-stack layer, n is number of piezo-stack layers in $PA_i(i = 1,2,3,4)$, d_{33} is the piezoelectric constant expressed with m/V or $Coulomb/Newton$.[40]

For actuating the proposed three-degree-of-freedom piezoelectric actuator in open loop, the relationship between the displacements of the CP along the X/Y/Z axes and the driving voltages of four piezo-stack actuators should be derived. In Fig. 2, the location of the vertex (Point V) of the end-effector when $U_i = \frac{U}{2}$ is chosen as the origin of Coordinate O–XYZ, and the locations of the CP labeled as P1 ~ P4 between the Mover and PA1 ~ PA4 are $P1(0, \frac{D_p}{2}, 0)$, $P2(0, \frac{-D_p}{2}, 0)$, $P3(\frac{-D_p}{2}, 0, 0)$, $P4(\frac{D_p}{2}, 0, 0)$, respectively. When PA1 ~ PA4 are actuated, the locations of P1 ~ P4 move to $P1(0, \frac{D_p}{2}, \delta z_1(t))$, $P2(0, \frac{-D_p}{2}, \delta z_2(t))$, $P3(\frac{-D_p}{2}, 0, \delta z_3(t))$, $P4(\frac{D_p}{2}, 0, \delta z_4(t))$ and the movement attitude of the Mover in Coordinate o–xyz can be calculated by

$$\begin{cases} z(t) = \dfrac{\delta z_1(t) + \delta z_2(t)}{2} \equiv \dfrac{\delta z_3(t) + \delta z_4(t)}{2} \\ \theta_x(t) = \dfrac{\delta z_1(t) - \delta z_2(t)}{D_p} \\ \theta_y(t) = \dfrac{\delta z_3(t) - \delta z_4(t)}{D_p} \end{cases}, \tag{2}$$

where $z(t)$ is the displacement of the Mover along z axes and $\theta_x(t)/\theta_y(t)$ is the rotation angle of the Mover around ox/oy axes. To keep the Mover moving steadily during the actuating of PA1 ~ PA4, the sum of $\delta z_1(t)$ and $\delta z_2(t)$ should be kept identically equal to the sum of $\delta z_3(t)$ and $\delta z_4(t)$ as illustrated in Eq. (2).

The end-effector moves along with the Mover and the displacements of the CP with the Movable Part in Coordinate O–XYZ can be calculated as follows according to the basic geometrical relationship,

$$\begin{cases} X_{CP}(t) = L \times \theta_y(t) \\ Y_{CP}(t) = -L \times \theta_x(t) \\ Z_{CP}(t) = z(t) - L \times [1 - \cos\,\theta_x(t) \times \cos\,\theta_y(t)] \end{cases}, \tag{3}$$

where $\mathbf{P(t)} = [X_{CP}(t), Y_{CP}(t), Z_{CP}(t)]^T$ is the displacement vector of the CP in Coordinate O–XYZ, L is length of the end-effector, which is equal to the distance from O to o and always keeps constant. A vector of driving voltage is defined as $U = [U_1(t), U_2(t), U_3(t), U_4(t)]^T$ and it is assumed that a control vector $Q(t) = [q_1(t), q_2(t), q_3(t)]^T$ is defined as

$$\begin{bmatrix} q_1(t) \\ q_2(t) \\ q_3(t) \end{bmatrix} = \begin{bmatrix} 1 & 1 & 0 & 0 \\ 1 & -1 & 0 & 0 \\ 0 & 0 & 1 & -1 \end{bmatrix} \times \begin{bmatrix} \delta z_1(t) \\ \delta z_2(t) \\ \delta z_3(t) \\ \delta z_4(t) \end{bmatrix} \Leftrightarrow \mathbf{Q(t)} = \mathbf{T_{z-q}} \times \mathbf{U(t)}, \tag{4}$$

$$\begin{bmatrix} q_1(t) \\ q_2(t) \\ q_3(t) \end{bmatrix} = \begin{bmatrix} n\Delta ld_{33} & -n\Delta ld_{33} & 0 & 0 \\ n\Delta ld_{33} & -n\Delta ld_{33} & 0 & 0 \\ 0 & 0 & n\Delta ld_{33} & -n\Delta ld_{33} \end{bmatrix} \times \begin{bmatrix} \delta U_1(t) \\ \delta U_2(t) \\ \delta U_3(t) \\ \delta U_4(t) \end{bmatrix} \Leftrightarrow \mathbf{Q(t)} = \mathbf{T_{u-z}} \times \mathbf{U(t)}, \tag{5}$$

where $U_i(t)$ has been defined in Eq. (1), matrix $\mathbf{T_{z-q}}$ defines the transformation between the control vector and displacement vector of the CP and matrix $\mathbf{T_{u-z}}$ defines the transformation between the control vector and driving voltage of PA1 ~ PA4. Considering that $\theta_x(t)$ and $\theta_y(t)$ are both sufficiently small, which means that $\cos\theta_x(t) \times \cos\theta_y(t) \approx 1$, then the displacement Vector $\mathbf{P(t)} = [X_{CP}(t), Y_{CP}(t), Z_{CP}(t)]^T$ can be derived from Eqs. (1)–(5) as follows:

$$\begin{aligned} \mathbf{P(t)} &= \begin{bmatrix} 0 & 0 & L \\ 0 & -L & 0 \\ 1 & 0 & 0 \end{bmatrix} \times \begin{bmatrix} \frac{1}{2} & 0 & 0 \\ 0 & \frac{1}{D_p} & 0 \\ 0 & 0 & \frac{1}{D_p} \end{bmatrix} \times \mathbf{Q(t)} \Leftrightarrow \mathbf{P(t)} \\ &= \mathbf{J_{m-p}} \times \mathbf{J_{q-m}} \times \mathbf{Q(t)}, \end{aligned} \tag{6}$$

where $\mathbf{J_{q-m}}$ is the transformation matrix from the control vector to the movement attitude of the Mover and $\mathbf{J_{m-p}}$ is the transformation matrix from the movement attitude to the displacement vector of the CP, the diagonal transformation matrix indicates that the Mover has decoupled movement attitude for $z(t)$, $\theta_x(t)$ and $\theta_y(t)$, and the CP has three decoupled translational degrees of freedom along X, Y and Z axes.

III. STIFFNESS MODELING AND DYNAMIC ANALYSIS

To analyze the dynamic characteristics of the proposed actuator, the stiffness of the spatial compliant mechanism is analytically modeled using the compliance matrix method[41–44] firstly, and then the natural frequencies of the three-degree-of-freedom actuator are derived with Lagrange's equations,[45] the accuracy of modeling and analysis is validated by finite element analysis method finally.

According to elastic beam theory, the static characteristics of multi-axis flexure hinges can be described by the compliance matrix,[46] and the compliance matrix of a parallel flexure mechanism is

$$C_p = \left(\sum_{i=1}^{n} ([Ad_i] C_{pi} [Ad_i]^T)^{-1} \right)^{-1}, \tag{7}$$

where $Ad_i = \begin{bmatrix} \mathbf{R_i} & 0 \\ \hat{\mathbf{T}}_\mathbf{i} R_i & R_i \end{bmatrix}$ is the coordinate transformation matrix from a local element i to the global system; $\mathbf{R_i}$ is a 3×3 rotation matrix, $\hat{\mathbf{T}}_\mathbf{i} = \begin{bmatrix} 0 & -z_i & y_i \\ z_i & 0 & -x_i \\ -y_i & x_i & 0 \end{bmatrix}$ is skew-symmetric matrix defined by a translation vector $\mathbf{T_i} = [x_i y_i z_i]$.

The proposed actuator is driven by four piezo-stack actuator PA1 ~ PA4, which are guided and preloaded with an annular plate, a flexible, rod and multiple Belleville Springs. The annular plate is parallelly connected with the flexible rod in space and then serially connected with the Belleville Springs in Z direction. Then, the compliance matrix of the guiding mechanism composed by the annular plate and the flexible rod in the global actuator coordinate o–xyz in Fig. 2 can be calculated by

$$\begin{aligned} \mathbf{C_{guiding}} = \Big(&([Ad_{plate}] \mathbf{C_{plate}} [Ad_{plate}]^T)^{-1} \\ &+ ([Ad_{rod}] \mathbf{C_{rod}} [Ad_{rod}]^T)^{-1} \Big)^{-1}, \end{aligned} \tag{8}$$

where $\mathbf{C_{plate}}$ and $\mathbf{C_{rod}}$ are the compliance matrix of the annular plate and the flexible rod, respectively, in the local element coordinate frame, $[Ad_{plate}]$ and $[Ad_{rod}]$ are the so-called 6×6 adjoint transformation matrix of the annular plate and the flexible rod.[43,44]

For the annular plate with outer ring fixed and inner ring connected to a movable body, the local element coordinate O_p–$x_p y_p z_p$ originates at the center of the plate as sketched in Fig. 3, the compliance matrix of the annular plate is calculated as follows by dividing the plate into multiple identical sheet flexures[43,44] with bases fixed on the circumference of the outer ring and the movable body parallelly

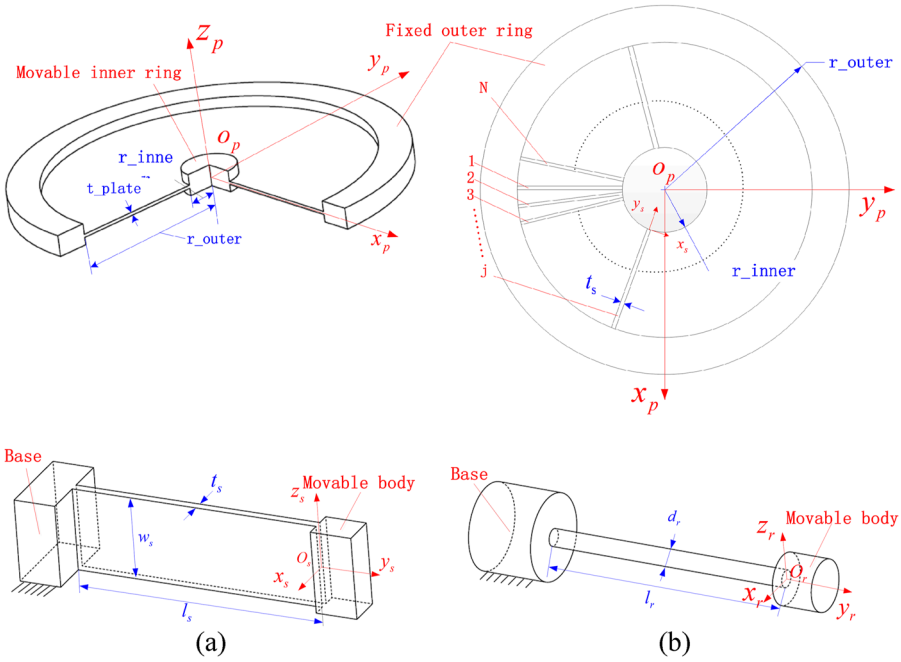

FIG. 3. Diagram of annular plate divided into multiple sheet flexures.

FIG. 4. Two types of basic flexible beams. (a) Sheet flexure; (b) flexible rod.

connected at the origin of coordinate O_p–$x_p y_p z_p$ as shown in Figs. 3 and 4(a),

$$\mathbf{C_{plate}} = \left(\sum_{j=1}^{N} ([Ad_{sheet-j}] C_{sheet-j} [Ad_{sheet-j}]^T)^{-1} \right)^{-1}, \tag{9}$$

where $C_{sheet-j}$ is the compliance matrix of the *jth* sheet flexure in local element coordinate frame and $Ad_{sheet-j}$ is the transformation matrix of the *jth* sheet flexure from the coordinate O_p–$x_p y_p z_p$ to its local element coordinate frame, N is the total number of sheet flexures into which the annular plate is divided as shown in Fig. 3.

Then, the calculation of the compliance matrix of the guiding mechanism composed by the annular plate and the flexible rod can be turned into the calculation of the compliance matrices of a commonly used sheet flexure and a flexible rod, which have been already derived in papers.[43,44] For convenience, the compliance matrix of the sheet flexure of which the local element coordinate O_s–$x_s y_s z_s$ locates at the free end of the beam in Fig. 4(a) is listed as follows:

$$\mathbf{T} = [C_s] \times \mathbf{W} \Leftrightarrow \begin{bmatrix} \delta x_s \\ \delta y_s \\ \delta z_s \\ \theta_{x_s} \\ \theta_{y_s} \\ \theta_{z_s} \end{bmatrix} = \begin{bmatrix} \frac{l_s^3}{3EI_{z_s}} & 0 & 0 & 0 & 0 & -\frac{l_s^2}{2EI_{z_s}} \\ 0 & \frac{l_s}{EA} & 0 & 0 & 0 & 0 \\ 0 & 0 & \frac{l_s^3}{3EI_{x_s}} & \frac{l_s^2}{2EI_{x_s}} & 0 & 0 \\ 0 & 0 & \frac{l_s^2}{2EI_{x_s}} & \frac{l_s}{2EI_{x_s}} & 0 & 0 \\ 0 & 0 & 0 & 0 & \frac{l_s}{G\beta_{z_s}} & 0 \\ -\frac{l_s^2}{2EI_{z_s}} & 0 & 0 & 0 & 0 & -\frac{l_s}{EI_{z_s}} \end{bmatrix} \times \begin{bmatrix} F_{x_s} \\ F_{y_s} \\ F_{z_s} \\ M_{x_s} \\ M_{y_s} \\ M_{z_s} \end{bmatrix}, \tag{10}$$

where $A = t_s \times w_s$ is the area of the rectangular cross-section, $I_{x_s} = \frac{t_s w_s^3}{12}$ and $I_{z_s} = \frac{t_s^3 w_s}{12}$ are the area moment, E is the Young's modulus, $G = \frac{E}{2(1+v)}$ is the shear modulus and v is the Passion's ratio. $\beta = 12\left(\frac{1}{3} - 0.21\frac{t_s}{w_s}\left(1 - \frac{1}{12}\left(\frac{t_s}{w_s}\right)^4\right)\right)$ is the ratio of torsion constant over the moment of inertia for a rectangular cross-section.[47] The compliance matrix of the flexible rod with its local element coordinate O_r–$x_r y_r z_r$ locating at the free end of the beam in Fig. 4(b) is listed as follows:

$$\mathbf{T} = [C_{rod}] \times \mathbf{W} \Leftrightarrow \begin{bmatrix} \delta x_r \\ \delta y_r \\ \delta z_r \\ \theta_{x_r} \\ \theta_{y_r} \\ \theta_{z_r} \end{bmatrix} = \begin{bmatrix} \frac{64l_r^3}{3\pi E d_r^4} & 0 & 0 & 0 & 0 & -\frac{32l_r^2}{\pi E d_r^4} \\ 0 & \frac{4l_r}{\pi E d_r^2} & 0 & 0 & 0 & 0 \\ 0 & 0 & \frac{64l_r^3}{3\pi E d_r^4} & \frac{32l_r^2}{\pi E d_r^4} & 0 & 0 \\ 0 & 0 & \frac{32l_r^2}{\pi E d_r^4} & \frac{64l_r}{\pi E d_r^4} & 0 & 0 \\ 0 & 0 & 0 & 0 & \frac{32l_r}{\pi G d_r^4} & 0 \\ -\frac{32l_r^2}{\pi E d_r^4} & 0 & 0 & 0 & 0 & \frac{64l_r}{\pi E d_r^4} \end{bmatrix} \times \begin{bmatrix} F_{x_r} \\ F_{y_r} \\ F_{z_r} \\ M_{x_r} \\ M_{x_r} \\ M_{z_r} \end{bmatrix}. \tag{11}$$

T = (δ; θ) is the deformation twist and **W** = (**F**; **M**) is the load wrench in Eqs. (10) and (11).

The calculating accuracy of the compliance matrix of the annular plate by dividing it into multiple identical sheet flexures depends heavily on the division number N, so the relationship between the calculating accuracy and the division number of basic sheet flexure is studied firstly considering specific structural parameters in Table I.

By substituting the compliance matrix of the sheet flexure C_s into Eq. (9) with specific parameters and transformation matrices listed in Table I, the compliance matrix of the annular plate $\mathbf{C_{plate}}$ can be derived as a 6 × 6 matrix with $C_{plate}(j,j)$ on its diagonal. Then, the relationship between the division number N and the compliance values of $C_{plate}(j,j)$ when $j = 3, 4, 5$, which correspond to the three degrees of freedom of the Mover, was studied with the structural parameters in Table I and shown in Fig. 5. Concluding from Fig. 5, the compliance values of $C_{plate}(j,j)$ when $j = 3, 4, 5$ tend to be convergent when the division number N is greater than 250. Then, $N = 300$ was chosen to approximately calculate the compliance matrix $\mathbf{C_{plate}}$ of the annular plate.

By substituting the compliance matrix of the annular plate $\mathbf{C_{plate}}$ when N = 300 and the compliance matrix of the flexible plate described in Eq. (11) with specific parameters and transformation matrix listed in Table I and considering the serially connected relationship in the Z direction between the guiding mechanism and the Belleville Springs, the compliance matrix $\mathbf{C_{guiding}}$ of the guiding mechanism for the proposed actuator can be calculated out and the stiffness with respect to the three degrees of freedom of the proposed actuator can be obtained as follows:

$$\begin{cases} K_z = \dfrac{1}{C_{guiding}(3,3) + \frac{1}{K_{pre}}} \\ K_{\theta_x} = \dfrac{1}{C_{guiding}(4,4)} \\ K_{\theta_y} = \dfrac{1}{C_{guiding}(4,4)} \end{cases}, \tag{12}$$

TABLE I. Structural parameters and corresponding transformation matrix.

Flexure type	Annular plate			Sheet flexure			Flexible rod		
Structural parameters	Name	Symbol	Value/m	Name	Symbol	Value/m	Name	Symbol	Value/m
	Inner radius	*r_inner*	0.002	Thickness of sheet j	t_s	$\frac{\pi\times(r\_inner+r\_outer)}{N}$	Length	l_r	0.018
	Outer radius	*r_outer*	0.015	Width of sheet j	$w_s = t\_plate$	0.0003	Diameter	d_r	0.0012
	Thickness	*t_plate*	0.0003	Orientation of sheet j	θ_j	$\frac{360\times j}{N}$			
	Young's modulus E = 2.0×10^{11}, Passion's ratio $\nu = 0.29$								
Transformation matrix	$\mathbf{R_{plate}} = \begin{bmatrix} 1 & 0 & 0 \\ 0 & 1 & 0 \\ 0 & 1 & 0 \end{bmatrix}$			$\mathbf{R_{sheet-j}} = \mathbf{R}(\mathbf{z_p}, \boldsymbol{\theta_j}) = \begin{bmatrix} \cos\theta_j & -\sin\theta_j & 0 \\ \sin\theta_j & \cos\theta_j & 0 \\ 0 & 0 & 1 \end{bmatrix}$			$\mathbf{R_{rod}} = R(X, 90^\circ) = \begin{bmatrix} 0 & 1 & 0 \\ 1 & 0 & 0 \\ 0 & 0 & 1 \end{bmatrix}$		
	$\mathbf{T_{plate}} = [0 \quad 0 \quad 0]$			$\mathbf{T_{sheet-j}} = [-r\_inner \times \cos\boldsymbol{\theta_j} \quad -r\_inner \times \sin\boldsymbol{\theta_j} \quad 0]$			$\mathbf{T_{rod}} = [\mathbf{0} \quad \mathbf{0} \quad \mathbf{-0.0015}]$		

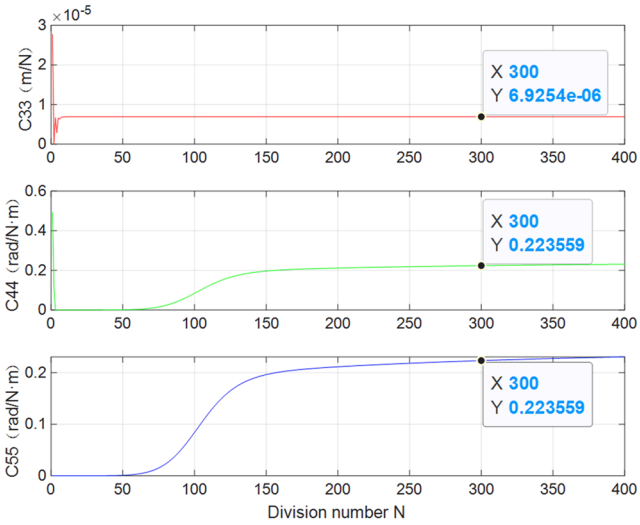

FIG. 5. Calculating of Compliance value with the increasing of division number.

where $C_{guiding}(j,j)(j=1,2,\ldots,6)$ are the elements on the diagonal of the calculated $\mathbf{C_{guiding}}$, K_z is the stiffness when the Mover moves in z direction, K_{pre} is the stiffness of the Belleville Springs as shown in Fig. 1, $K_{\theta_x}/K_{\theta_y}$ is the stiffness when the Mover rotates around the ox/oy axes.

When describing the free vibrations of the three-degree-of-freedom actuator, the movement attitude variables $\mathbf{A}=[A_1,A_2,A_3]=[z,\theta_x,\theta_y]$ of the Mover are chosen as the generalized coordinates. Since compliant mechanisms are used in the proposed actuator, there are no frictions in the structure, and thus the damping is neglected in the following analysis. As shown in Figs. 1(c) and 1(d), neglecting the tiny gravitational potential energy change, the potential energy of the actuator can be calculated by

$$V=\frac{1}{2}K_z z^2+\frac{1}{2}K_{\theta_x}\theta_x^2+\frac{1}{2}K_{\theta_y}\theta_y^2, \tag{13}$$

and the Kinetic energy of the Mover can be calculated by

$$T=\frac{1}{2}m\dot{z}^2+\frac{1}{2}J_x\dot{\theta}_x{}^2+\frac{1}{2}J_y\dot{\theta}_y{}^2, \tag{14}$$

where m is the mass of the Mover, J_x and J_x are moments of inertia of the Mover.

Substitute the kinetic and potential energy into Lagrange's equations as follows when there are no non-conservative forces,

$$\frac{d}{dt}\frac{\partial T}{\partial \dot{A}_i}-\frac{\partial T}{\partial A_i}+\frac{\partial V}{\partial A_i}=0. \tag{15}$$

The dynamic equations of the actuator can be derived as follows:

$$\begin{bmatrix} m & 0 & 0\\ 0 & J_x & 0\\ 0 & 0 & J_y\end{bmatrix}\times\begin{bmatrix}\ddot{z}\\ \ddot{\theta}_x\\ \ddot{\theta}_y\end{bmatrix}+\begin{bmatrix} K_z & 0 & 0\\ 0 & K_{\theta_x} & 0\\ 0 & 0 & K_{\theta_y}\end{bmatrix}\times\begin{bmatrix} z\\ \theta_x\\ \theta_y\end{bmatrix}=0$$
$$\Leftrightarrow \mathbf{M}\times\begin{bmatrix}\ddot{z}\\ \ddot{\theta}_x\\ \ddot{\theta}_y\end{bmatrix}+\mathbf{K}\times\begin{bmatrix} z\\ \theta_x\\ \theta_y\end{bmatrix}=0 \tag{16}$$

Then, according to the characteristic equation

$$|\mathbf{K}-\mathbf{M}\lambda_i^2|=0. \tag{17}$$

The first three natural frequencies of the proposed actuator can be calculated by

$$f_i=\frac{\lambda_i}{2\pi}, \tag{18}$$

where $i=1,2,3$ in Eqs. (15)–(18).

The first three natural frequencies of the proposed actuator were also calculated with finite element analysis (FEA) in ANSYS/Workbench, the FEA results are shown in Fig. 6 and compared with the analytical results as listed in Table II.

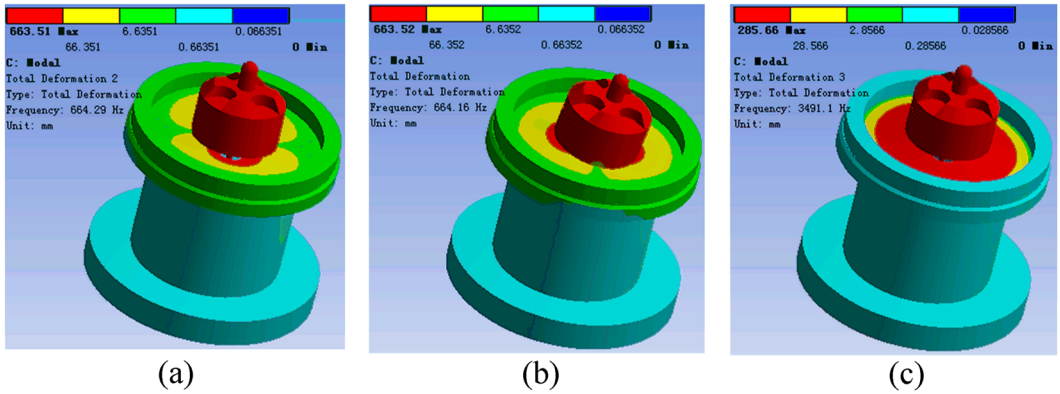

FIG. 6. FEA Modal. (a) Mode of θ_x; (b) Mode of θ_y; and (c) Mode of z.

TABLE II. Comparison of Modal results with specific parameters.

MODAL	Analytical Result	FEA result	Difference (%)	Mover parameter
First-order mode/Hz	649.05	664.16	2.33	$m = 5.692 \times 10^{-3}$ kg
Second-order mode/Hz	649.05	664.29	2.35	$J_x = 4.96 \times 10^{-7}$ kg m^2
Third-order mode/Hz	3328.29	3491.10	4.89	$J_y = 4.9696 \times 10^{-7}$ kg m^2

The differences between the analytical and FEA modal results are less than 5%, which validates the correctness and accuracy of the stiffness modeling and the free vibration analysis for the proposed actuator.

IV. EXPERIMENT RESULT

A. Experiment platform configuration

A prototype of the proposed three-degree-of-freedom actuator is fabricated and tested as shown in Fig. 7. A signal generator developed with Labview in computer generates four-channel driving voltage of 0 ~ 10 V through a Digital-to-Analogue card (NI-6154, National Instruments Corp., Germany). The four-channel voltage signals are amplified by a commercial Amplifier (TD250, Piezo-Drive, Canada) and finally applied to actuate the prototype actuator. Three capacitive sensors (CSH05, Micro-Epsilon, Germany) are used to measure the attitude of the stator when the Mover is fixed to the mounting connector, since it would be more difficult to directly measure the displacement of the CP on its end-effector, which is removed in the prototype actuator in Fig. 7. The displacement values of the capacitive sensors are electronically processed by a signal conditioner (capaNCDT 6500, Micro-Epsilon, Germany) and sampled through an Analogue-to-Digital card (PCI-9524, ADLINK TECHNOLOGY, INC.) with 1000 Hz sampling frequency, the sampling

FIG. 7. Experimental platform configuration.

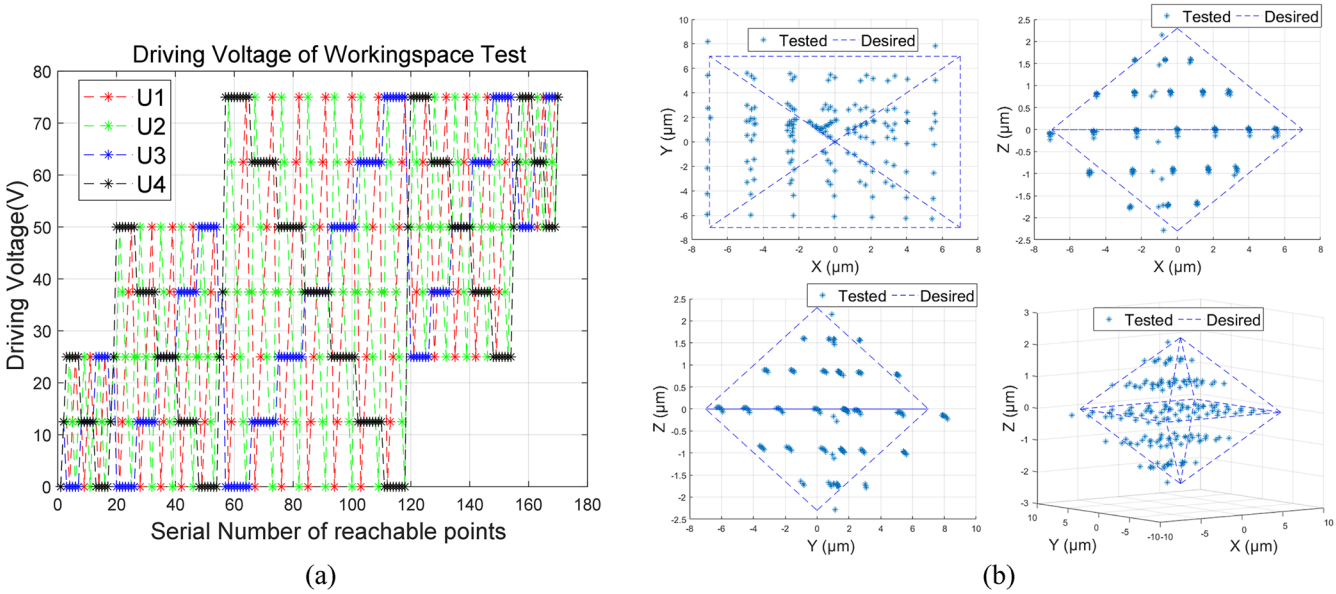

FIG. 8. Working space test of the prototype actuator. (a) Driving voltage; (b) tested working space.

data are then processed programmatically with Matlab in Computer. The prototype actuator and the capacitive sensors are fixed on a vibration isolation platform (VC-D) through the mounting connector, and the temperature in the laboratory is controlled within $22 \pm 0.5\,^{\circ}\mathrm{C}$.

The relationship between the attitude of the Mover and the displacement changes of the sensors can be calculated as follows according to basic geometry correlation in coordinate O–XYZ,

$$\begin{bmatrix} z \\ \theta_x \\ \theta_y \end{bmatrix} = \begin{bmatrix} -z_{stator} \\ -\theta_{x-stator} \\ -\theta_{y-stator} \end{bmatrix} = \begin{bmatrix} -\frac{1}{3} & -\frac{1}{3} & -\frac{1}{3} \\ 0 & \frac{\sqrt{3}}{3r} & -\frac{\sqrt{3}}{3r} \\ \frac{2}{3r} & -\frac{1}{3r} & -\frac{1}{3r} \end{bmatrix} \begin{bmatrix} \Delta S1 \\ \Delta S2 \\ \Delta S3 \end{bmatrix}, \tag{19}$$

where $\Delta S1, \Delta S2$, and $\Delta S3$ are the displacement changes of Sensor 1 ~ Sensor 3, $r = 5$ mm is the distance from the center axis of the sensor to the center axis of the proposed actuator and $\begin{bmatrix} z_{stator} \\ \theta_{x-stator} \\ \theta_{y-stator} \end{bmatrix}$ is the attitude of the stator. Then, the displacement of the prototype actuator, which is concerned in this paper, can be calculated out by substituting Eq. (19) into Eq. (3).

B. Output performance evaluation

The output performances of the prototype actuator, including working space, translational displacement resolutions, motion speed, and carrying capability, were tested, respectively.

First, the working space of the prototype actuator was tested. A total of 170 representative points, seemingly contained within the

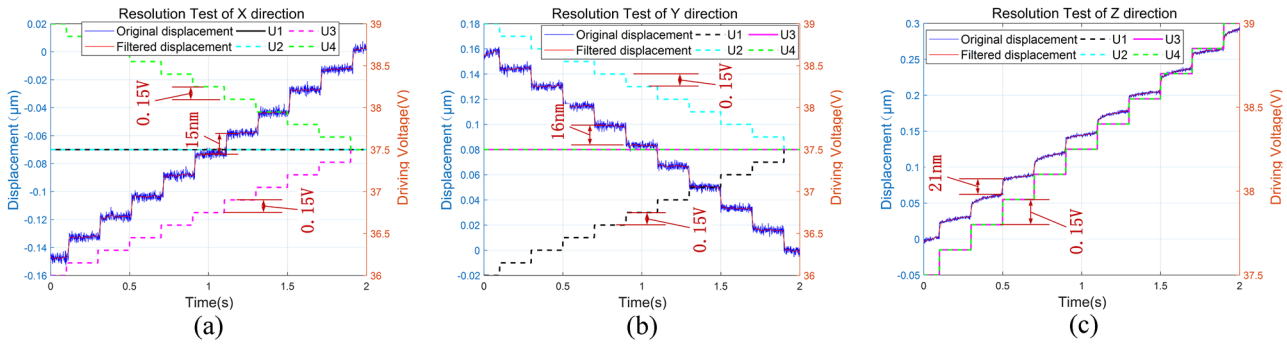

FIG. 9. Resolution test of the prototype actuator. (a) Resolution test of X direction; (b) Resolution test of Y direction; and (c) Resolution test of Z direction.

space of two opposing tetragonal pyramid in Fig. 8(b), are verified to be reachable with corresponding driving voltage as shown in Fig. 8(a). The tested working space with X range of −7.1 ~ 5.6 μm, Y range of −6.2 ~ 8.2 μm and Z range of −2.3 ~ 2.1 μm is asymmetrical and has some deviations compared with the desired working space within the blue dashed line in Fig. 8(b), which are probably caused by hysteresis effect and assembling errors of four piezo-stack actuators.

Second, driving signals of stepping voltage were applied to the prototype actuator to test the resolutions of displacement. The increment of stepping voltage is 0.15 V and the driving frequency is 5 Hz, which equals to the inverse of the time interval of the stepping voltage. The displacement resolutions along X-axis, Y-axis, and Z-axis were measured and filtered with a moving-average filter as shown in Fig. 9. The results show that displacement resolutions of 15 nm along X-axis, 16 nm along Y-axis and 21 nm along Z-axis have been achieved by the prototype actuator.

Third, the motion speed and carrying capability were tested to investigate the relationship between the output average velocity and the driving frequency under different load conditions, Standard weights of 0.5 ~ 2 Kg were utilized to add load through load transmission mechanism as shown in Fig. 10(d), the weights are bonded with one end of a stainless steel shaft, the shaft is guided by a linear bearing, which is bonded with the Sensor Holder, the other end of the shaft are then pressed to a stainless steel hemisphere, which is bonded with the proposed actuator to provide a single contact point with the shaft, then the output velocities corresponding to the three degrees of the proposed actuator were tested under different load conditions and different driving frequencies. The test results indicate that the average velocities of the prototype actuator along X-axis,

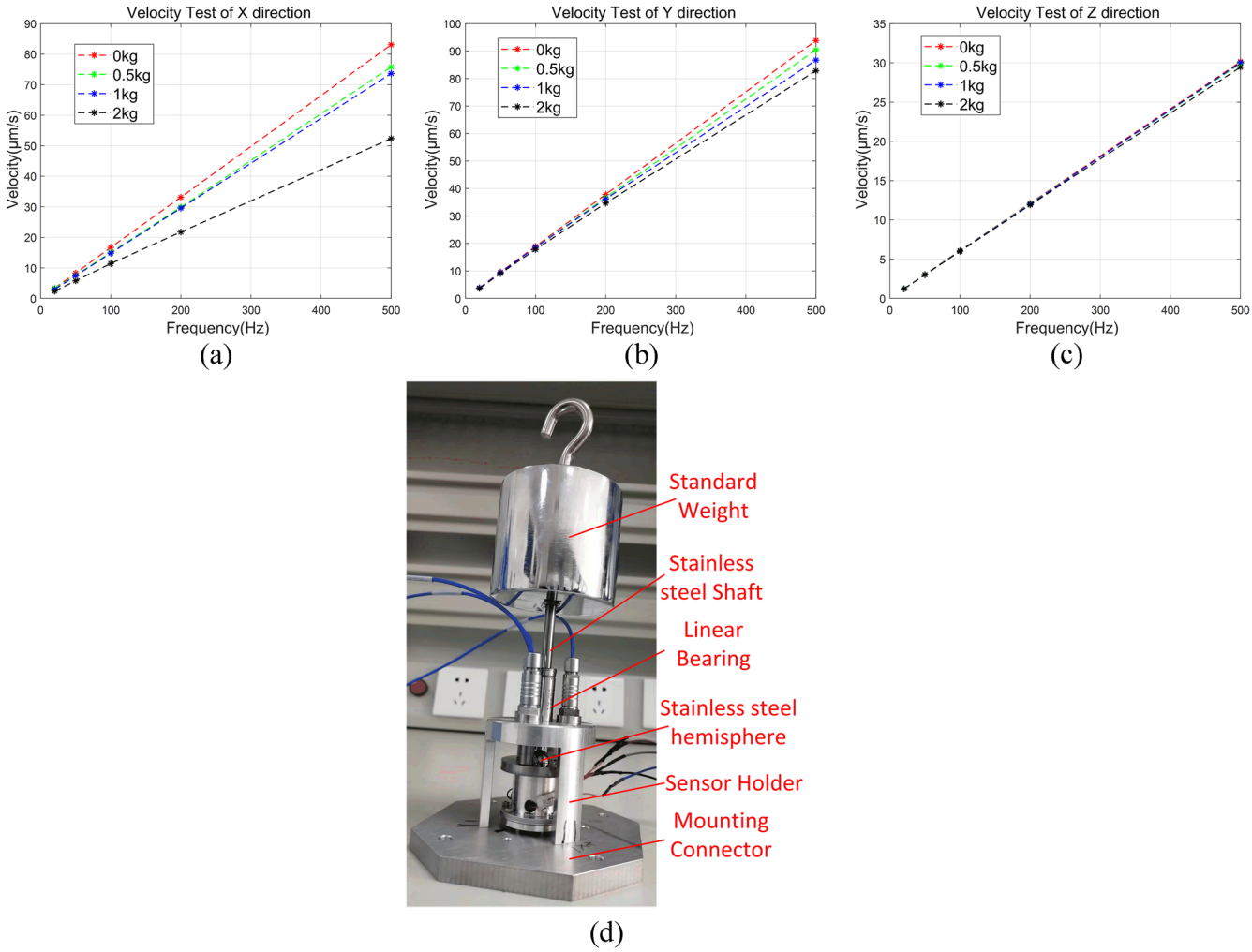

FIG. 10. Velocity test of the prototype actuator. (a) Velocity test of X direction; (b) velocity test of Y direction; (c) velocity test of Z direction; and (d) platform of load capacity test.

Y-axis, and Z-axis increase linearly with the increasing driving frequency under fixed load conditions as shown in Figs. 10(a)–10(c), respectively, and with the increment of the applied load, the average velocities along X-axis, Y-axis, and Z-axis decrease to different level under fixed driving frequency. Compared with the zero-load condition, the average velocities reduce by about 36% along X-axis, about 12% along Y-axis, and about 2% along Z-axis under 2 Kg load condition, and the different reduction percentages are caused probably by alignment errors of the piezo-stack actuators and modal differences along different working axis. The test results also indicate that with a carrying load up to 2 kg and driving frequency of 500 Hz, average velocities of 52.3 μm/s along X-axis, 82.8 μm/s along Y-axis and 29.5 μm/s along Z-axis have been achieved by the proposed actuator.

C. Waveform generating with hysteresis compensation

To be further used to drive a large and heavy mirror as shown in Fig. 1 with the clamping and feeding mode, trajectory tracking performance of the proposed actuator was investigated. The method of generating the waveform of driving voltage for a desired trajectory has been developed with inverse hysteresis compensation, and the positioning accuracy has been improved observably in different trajectory tracking of the prototype actuator.

The output displacements of PA1 ~ PA4 (PTH1500525051, PANT, China) with input driving voltage range of 0 ~75 VDC were measured, respectively, by a capacitive sensor (CSH05, Micro-Epsilon, Germany) before assembling into the prototype actuator, PA1 ~ PA4 perform different hysteresis characteristics as shown in

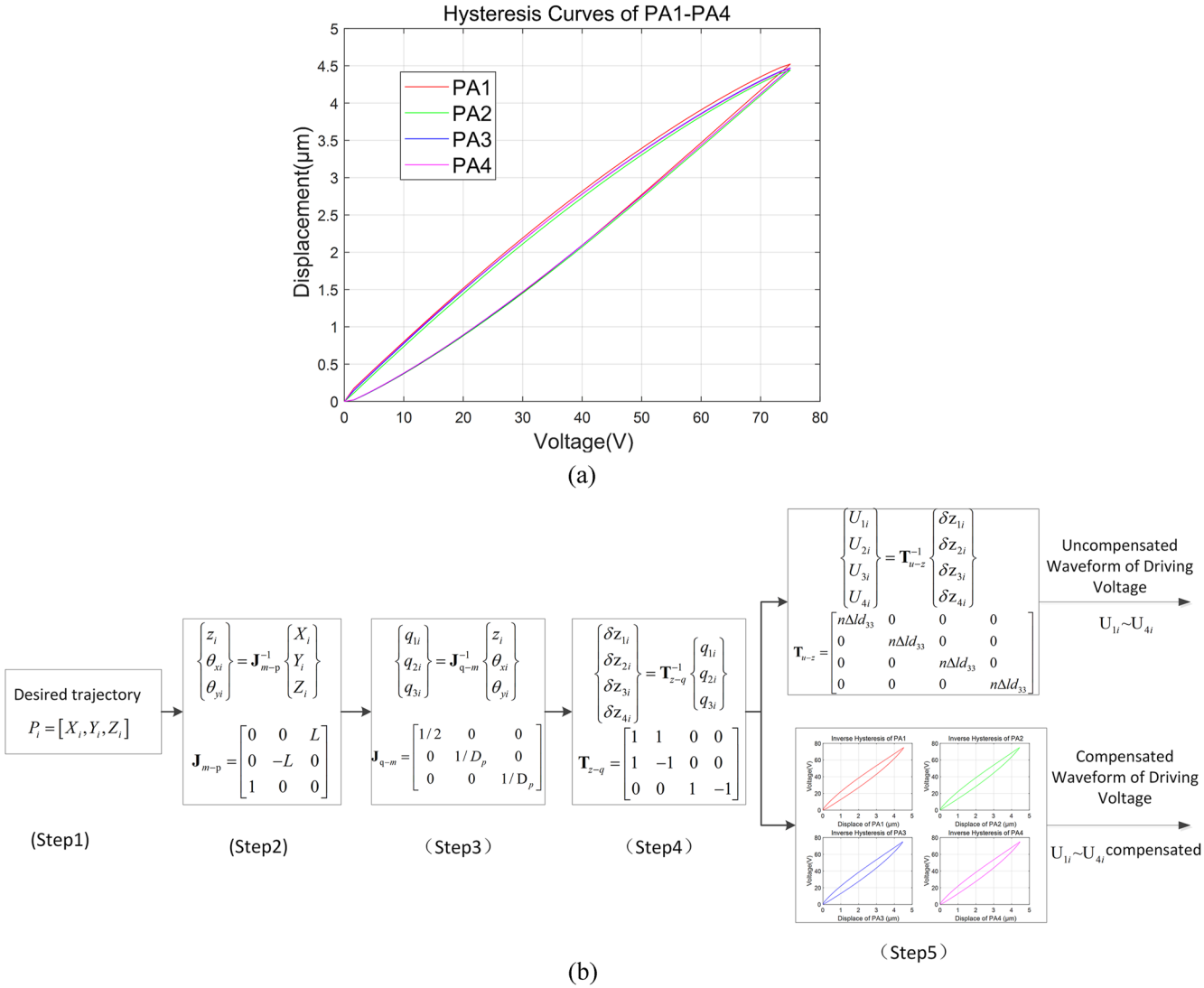

FIG. 11. Waveform generating with Hysteresis compensation. (a) Hysteresis curves of PA1 ~ PA4; (b) Algorithm diagram of waveform generating.

Fig. 11(a). The waveform of driving voltage was planned in advance according to the derived kinematic relationship between the four-channel input driving voltage and the output displacements of the proposed actuator in Part II of this paper, and the detailed algorithm is shown in Fig. 11(b) and illustrated as follows:

Step 1: A desired trajectory within the working space of the prototype actuator is expressed by a parameterized equation in polar coordinates.

Step 2–*Step* 4: The coordinates of the series of points representing the desired trajectory are transformed into the output displacements of the four piezo-stack actuators by the inverse of matrix $\mathbf{J_{m-p}}$ derived in Eq. (6), the inverse of matrix $\mathbf{J_{q-m}}$ derived in Eq. (6) and the inverse of matrix $\mathbf{T_{z-q}}$ derived in Eq. (4).

Step 5: The output displacements are transformed into the corresponding uncompensated waveform of input driving voltage for the proposed actuator by the inverse of matrix $\mathbf{T_{u-z}}$, which is derived in Eq. (5) and maps the linear relationship between the output displacements and driving voltage of four piezo-stack actuators without consideration of hysteresis effect. By replacing $\mathbf{T_{u-z}}$ with the corresponding tested inverse hysteresis relationship of PA1 ~ −PA4, the compensated waveform of driving voltage can be achieved to actuate the proposed actuator with higher positioning accuracy for the desired trajectory.

The planned uncompensated and compensated waveform of driving voltage are then loaded into the signal generator and amplified by an amplifier as illustrated in Fig. 7 to actuate the prototype actuator in an open loop.

Various types of trajectory tracking have been tested and evaluated. While evaluating the trajectory tracking performance, the position errors between two points $P_{i,desired} = [X_{i,desired}, Y_{i,desired}, Z_{i,desired}]$ and $P_{i,tested} = [X_{i,tested}, Y_{i,tested}, Z_{i,tested}]$ in coordinate O–XYZ are defined as follows:

$$\begin{cases} \Delta X_i = X_{i,tested} - X_{i,desired} \\ \Delta Y_i = Y_{i,tested} - Y_{i,desired} \\ \Delta Z_i = Z_{i,tested} - Z_{i,desired} \end{cases}. \tag{20}$$

Distance error between these two points is defined as follows:

$$d_{i,XYZ} = \sqrt{\Delta X_i^2 + \Delta Y_i^2 + \Delta Y_i^2}, \tag{21}$$

where $i = 1, 2, 3, \ldots, M$ and M is the total number of points utilized to represent a desired trajectory. The position error and the distance error are utilized to evaluate the positioning accuracy of the prototype actuator in open-loop control mode.

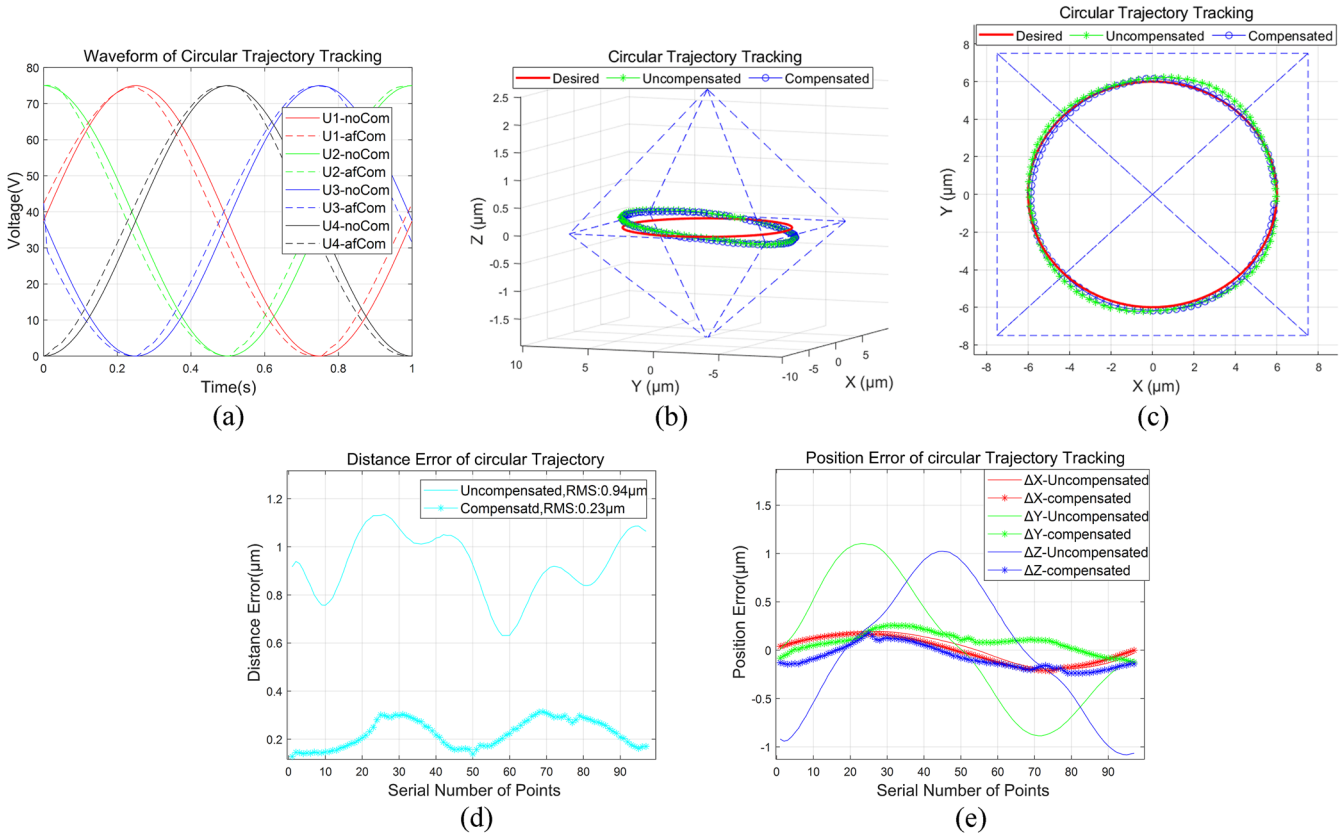

FIG. 12. Circular trajectory tracking in plane XY. (a) The waveform of driving voltage; (b) 3D view of circular trajectory tracking; (c) top view of circular trajectory tracking; (d) test result of distance error; and (e) test result of position errors.

First, a circular trajectory tracking in plane XY has been planned and tested as shown in Fig. 12. With the waveform of input driving voltage for PA1 ~ PA4 shown in Fig. 12(a), the prototype actuator can be controlled in open loop to track the circular trajectory in plane XY as shown in Figs. 12(b) and 12(c). The expected circular trajectory is represented by 100 points, the distance error and the position errors of the tested uncompensated and compensated trajectory tracking are shown in Figs. 12(d) and 12(e). Compared with the root-mean-square (rms) value of the distance error of the uncompensated circular trajectory tracking, the rms value of distance error of the compensated circular trajectory tracking falls from 0.94 to 0.23 μm, which indicates that the positioning accuracy of the prototype actuator has been observably improved.

The test results also show that most of the decrease of distance error comes from the decreases of the position errors ΔX and ΔY. The position error of ΔZ originating from the rotation of Theta-X and Theta-Y has not been considered in this paper and the compensation of ΔZ will also improve the positioning accuracy of the actuator in this circular trajectory tracking, which will be investigated in the future study.

Second, an elliptical trajectory tracking in plane XZ has been planned and tested as shown in Fig. 13. With the waveform of input driving voltage for PA1 ~ −PA4 in Fig. 13(a), the prototype actuator can be controlled in open loop to track the elliptical trajectory in plane XZ as shown in Figs. 13(b) and 13(c). The desired elliptical trajectory is represented by 100 points, the distance error and the position errors of tested uncompensated and compensated trajectory tracking are shown in Figs. 13(d) and 13(e). Compared with the rms value of distance errors of the uncompensated elliptical trajectory, the rms value of distance errors of the compensated elliptical trajectory falls from 0.48 to 0.29 μm, which comes from the decreases of position errors of $\Delta X, \Delta Y$ and ΔZ. With compensated waveform of driving voltage, the positioning accuracy has also been improved for the elliptical trajectory tracking of the prototype actuator.

Third, an rectangular trajectory tracking in space has been planned and tested as shown in Fig. 14. With the waveform of input driving voltage for PA1 ~ PA4 in Fig. 14(a), the prototype actuator can be controlled in open loop to track the rectangular trajectory as shown in Fig. 14(b). The desired rectangular trajectory is represented by 180 points, the distance error and the position errors of tested uncompensated and compensated trajectory tracking are shown in Figs. 14(c) and 14(d). Compared with rms value of distance error of the uncompensated rectangular trajectory tracking, the rms value of distance error of the compensated rectangular trajectory tracking falls from 0.61 to 0.32μm, which comes from the decreases of position errors of $\Delta X, \Delta Y$, and ΔZ as shown in Fig. 14(d). The

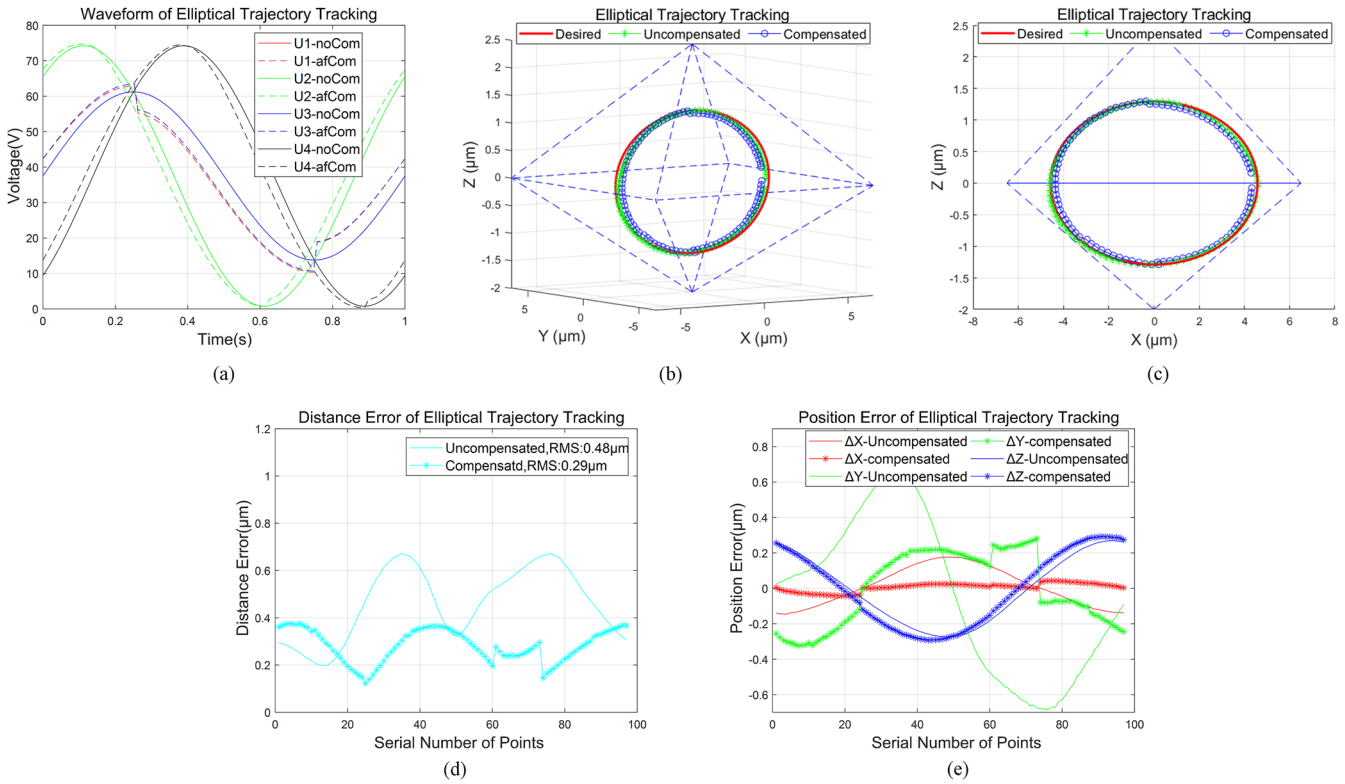

FIG. 13. Elliptical trajectory tracking in plane XZ. (a) The waveform of driving voltage; (b) 3D view of elliptical trajectory tracking; (c) Top view of elliptical trajectory tracking; (d) Test result of distance error; and (e) Test result of position errors.

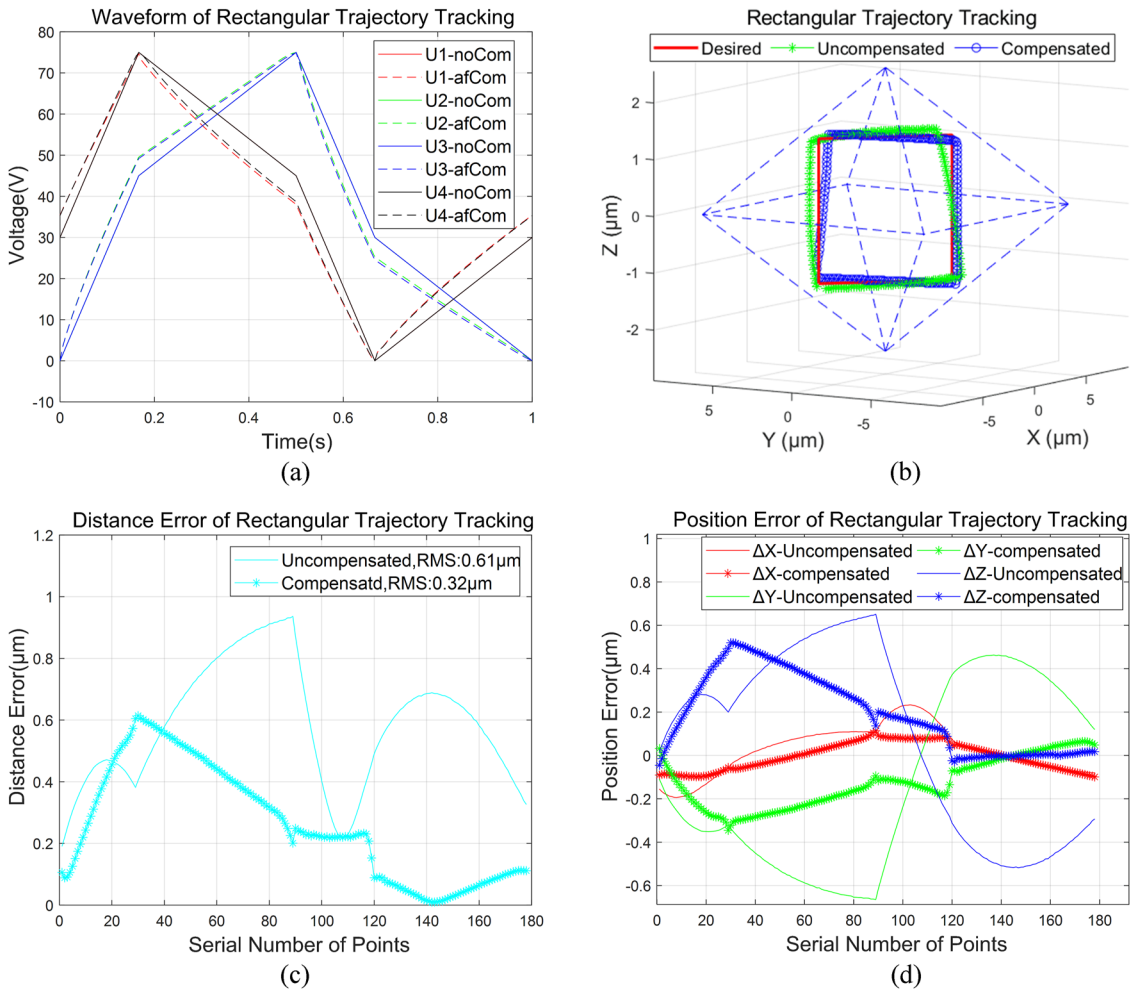

FIG. 14. Rectangular trajectory tracking in space. (a) The waveform of driving voltage; (b) 3D view of rectangular trajectory tracking; (c) Test result of distance error; and (d) test result of position errors.

positioning accuracy has been improved in the rectangular trajectory tracking of the prototype actuator.

The above tested results of trajectory tracking validate that with the inverse hysteresis compensation, the prototype actuator can be controlled in open loop to track different trajectories with positioning accuracy of sub-micrometer level, which established a foundation for the proposed three-degree-of-freedom piezoelectric actuator to be utilized to manipulate a large and heavy lens/mirror in the future investigation.

V. CONCLUSIONS

A novel three-degree-of-freedom piezoelectric actuator is designed, analyzed, fabricated, and tested. The structure and working principle of the proposed actuator are illustrated and its kinematic characteristics are analyzed. The stiffness of the spatial compliant mechanism is modeled, and the dynamic characteristics are analyzed, minor difference between the analytical and FEA modal result validate the correctness and accuracy of the modeling and the free vibration analysis for the proposed actuator. The output performances, including working space, displacement resolutions, motion speed, and carrying capability of the prototype actuator, have been tested, tested results show that the prototype actuator performs working space with X ranging from −7.1 to 5.6 μm, Y ranging from −6.2 to 8.2 μm and Z ranging from −2.3 to 2.1 μm, displacement resolutions of 15 nm along X-axis, 16 nm along Y-axis and 21 nm along Z-axis, and average velocities of 52.3 μm/s along X-axis, 82.8 μm/s along Y-axis and 29.5 μm/s along Z-axis with a carrying load up to 2 kg and driving frequency of 500 Hz. The method of waveform generating for the proposed actuator has been developed with the inverse hysteresis compensation, and the positioning accuracy of the prototype actuator has been improved from 0.94 to 0.23 μm for the circular trajectory tracking, from 0.48 to 0.29 μm for the elliptical trajectory tracking, and from 0.61 to 0.32 μm for the

rectangular trajectory with the compensated waveform of driving voltage, which establish a great foundation for the proposed actuator to be utilized to manipulate a large and heavy mirror/lens in the future study.

ACKNOWLEDGMENTS

This work was supported by the National Science and Technology Major Project (Grant No. 2016ZX02201) of China.

AUTHOR DECLARATIONS

Conflict of Interest

The authors have no conflicts to disclose.

Author Contributions

Fenglong Wei: Supervision (equal); Validation (equal); Writing – original draft (equal). **Xueliang Wang**: Methodology (equal); Supervision (equal). **Jingshi Dong**: Supervision (equal). **Kang Guo**: Methodology (equal); Supervision (equal). **Yongxin Sui**: Supervision (equal).

DATA AVAILABILITY

All data generated or used during the study are available from the corresponding author by resonable request.

REFERENCES

[1]X. Zhang, A. Senthil Kumar, M. Rahman, C. Nath, and K. Liu, "Experimental study on ultrasonic elliptical vibration cutting of hardened steel using PCD tools," J. Mater. Process. Technol. **211**, 1701–1709 (2011).
[2]F. Wang, H. Zhang, C. Liang, Y. Tian, X. Zhao, and D. Zhang, "Design of high-frequency ultrasonic transducers with flexure decoupling flanges for thermosonic bonding," IEEE Trans. Ind. Electron. **63**, 2304 (2016).
[3]W. Xu and Y. Wu, "Piezoelectric actuator for machining on macro-to-micro cylindrical components by a precision rotary motion control," Mech. Syst. Signal Process. **114**, 439–447 (2019).
[4]A. Matsubara, M. Maeda, and I. Yamaji, "Vibration suppression of boring bar by piezoelectric actuators and LR circuit," CIRP Ann. **63**, 373–376 (2014).
[5]D. Croft, G. Shed, and S. Devasia, "Creep, hysteresis, and vibration compensation for piezoactuators: Atomic force microscopy application," J. Dyn. Syst., Meas., Control **123**, 35 (2001).
[6]R. J. Hocken, N. Chakraborty, and C. Brown, "Optical metrology of surfaces," CIRP Ann. **54**, 169–183 (2005).
[7]W.-L. Zhu, Z. Zhu, P. Guo, and B.-F. Ju, "A novel hybrid actuation mechanism based XY nanopositioning stage with totally decoupled kinematics," Mech. Syst. Signal Process. **99**, 747–759 (2018).
[8]K. Cai, Y. Tian, X. Liu, S. Fatikow, F. Wang, L. Cui, D. Zhang, and B. Shirinzadeh, "Modeling and controller design of a 6-DOF precision positioning system," Mech. Syst. Signal Process. **104**, 536–555 (2018).
[9]W. Zhu, F. Yang, and X. Rui, "Robust independent modal space control of a coupled nano-positioning piezo-stage," Mech. Syst. Signal Process. **106**, 466–478 (2018).
[10]K. K. Leang and S. Devasia, "Feedback-linearized inverse feedforward for creep, hysteresis, and vibration compensation in AFM piezoactuators," IEEE Trans. Control Syst. Technol. **15**, 927–935 (2007).
[11]S. Tien, Q. Zou, and S. Devasia, "Iterative control of dynamics-coupling-caused errors in piezoscanners during high-speed AFM operation," IEEE Trans. Control Syst. Technol. **13**, 921–931 (2005).
[12]N. Bonnail, D. Tonneau, F. Jandard, G.-A. Capolino, and H. Dallaporta, "Variable structure control of a piezoelectric actuator for a scanning tunneling microscope," IEEE Trans. Ind. Electron. **51**, 354–363 (2004).
[13]S. Wang, W. Rong, L. Wang, H. Xie, L. Sun, and J. K. Mills, "A survey of piezoelectric actuators with long working stroke in recent years: Classifications, principles, connections and distinctions," Mech. Syst. Signal Process. **123**, 591–605 (2019).
[14]J. Li, H. Huang, and T. Morita, "Stepping piezoelectric actuators with large working stroke for nano-positioning systems: A review," Sens. Actuators, A **292**, 39–51 (2019).
[15]L. Wang, W. Chen, J. Liu, J. Deng, and Y. Liu, "A review of recent studies on non-resonant piezoelectric actuators," Mech. Syst. Signal Process. **133**, 106254 (2019).
[16]H. Bao, J. Wen, J. Ma, J. Zheng, and C. Kang, "An inertial piezoelectric hybrid actuator with large angular velocity and high resolution," in IEEE International Conference on Manipulation, Manufacturing and Measurement on the Nanoscale (3M-NANO), 2018.
[17]J.-W. Wu, K.-C. Huang, M.-L. Chiang, M.-Y. Chen, and L.-C. Fu, "Modeling and controller design of a precision hybrid scanner for application in large measurement-range atomic force microscopy," IEEE Trans. Ind. Electron. **61**, 3704–3712 (2014).
[18]S. Mohith, A. R. Upadhya, K. P. Navin, S. M. Kulkarni, and M. Rao, "Recent trends in piezoelectric actuators for precision motion and their applications: A review," Smart Mater. Struct. **30**, 013002 (2020).
[19]L. Wang, J. Liu, S. Chen, K. Li, and Y. Liu, "Design and fabrication of a high-speed linear piezoelectric actuator with nanometer resolution using a cantilever transducer," Smart Mater. Struct. **28**, 055035 (2019).
[20]J. Shields, "Asynchronous control of a prototype inchworm actuator: Control design and test results," Actuators **8**, 20 (2019).
[21]X. Ma, Y. Liu, J. Deng, X. Gao, and J. Cheng, "A compact inchworm piezoelectric actuator with high speed: Design, modeling, and experimental evaluation," Mech. Syst. Signal Process. **184**, 109704 (2022).
[22]J. Jungblut, J. Haas, and S. Rinderknecht, "A new active balancing device utilizing rotating piezo actuators," Mech. Syst. Signal Process. **181**, 109521 (2022).
[23]Z. Ding, J. Dong, X. Zhou, Z. Xu, W. Qiu, and C. Shen, "Achieving smooth motion of stick–slip piezoelectric actuator by means of alternate stepping," Mech. Syst. Signal Process. **181**, 109494 (2022).
[24]F. Wang, X. Zhao, Z. Huo, B. Shi, Y. Tian, and D. Zhang, "A novel large stepping-stroke actuator based on the bridge-type mechanism with asymmetric stiffness," Mech. Syst. Signal Process. **179**, 109317 (2022).
[25]F. Chen, Q. Zhang, W. Dong, and L. Sun, "Design and test of a compact large-stroke dual-drive linear-motion system," Mech. Syst. Signal Process. **180**, 109438 (2022).
[26]J. Ling, L. Chen, Z. Feng, and Y. Zhu, "Development and test of a high speed pusher-type inchworm piezoelectric actuator with asymmetric driving and clamping configuration," Mech. Mach. Theory **176**, 104997 (2022).
[27]Y. Liu, J. Deng, and Q. Su, "Review on multi-degree-of-freedom piezoelectric motion stage," IEEE Access **6**, 59986–60004 (2018).
[28]See https://www.physikinstrumente.com/en/ for PhysikInstrumente; accessed 11 September 2022.
[29]See http://piezomotor.com/linear-motors/ for PiezoMotor; accessed 11 September 2022.
[30]R. J. E. Merry, N. C. T. de Kleijn, M. J. G. van de Molengraft, and M. Steinbuch, "Using a walking piezo actuator to drive and control a high-precision stage," IEEE/ASME Trans. Mechatron. **14**, 21–31 (2009).
[31]M. den Heijer, V. Fokkema, A. Saedi, P. Schakel, and M. J. Rost, "Improving the accuracy of walking piezo motors," Rev. Sci. Instrum. **85**, 055007 (2014).
[32]R. Ryndzionek and Ł. Sienkiewicz, "A review of recent advances in the single- and multi-degree-of-freedom ultrasonic piezoelectric motors," Ultrasonics **116**, 106471 (2021).
[33]R. Bansevicius, G. Kulvietis, V. Jurenas, and J. Janutenaite-Bogdaniene, "Piezoelectric kinematic pairs with several DOF in miniature high-resolution piezoelectric robots," J. Vibro Eng. **19**, 5182–5190 (2017).

[34]C.-H. Cheng and S.-K. Hung, "A piezoelectric two-degree-of-freedom nanostepping motor with parallel design," IEEE/ASME Trans. Mechatron. **21**, 2197–2199 (2016).
[35]X. Sun, W. Chen, J. Zhang, Z. Rui, and W. Chen, "A novel piezo-driven linear-rotary inchworm actuator," Sens. Actuators, A **224**, 78 (2015).
[36]J. Li, H. Zhao, X. Qu, H. Qu, X. Zhou, Z. Fan, Z. Ma, and H. Fu, "Development of a compact 2-DOF precision piezoelectric positioning platform based on inchworm principle," Sens. Actuators, A **222**, 87–95 (2015).
[37]S. Zhang, J. Liu, J. Deng, and Y. Liu, "Development of a novel two-DOF pointing mechanism using a bending-bending hybrid piezoelectric actuator," IEEE Trans. Ind. Electron. **66**, 7861–7872 (2019).
[38]B. Arda Gozen and O. B. Ozdoganlar, "Characterization of three-dimensional dynamics of piezo-stack actuators," Mech. Syst. Signal Process. **31**, 268–283 (2012).
[39]See http://www.coremorrow.com/pro-88-1.html/ for COREMORROW; accessed 11 June 2022.
[40]A. Preumont, *Mechatronics: Dynamics of Electromechanical and Piezoelectric Systems* (Springer, Netherlands, 2006).
[41]M. Ling, L. L. Howell, J. Cao, and G. Chen, "Kinetostatic and dynamic modeling of flexure-based compliant mechanisms: A survey," Appl. Mech. Rev. **72**, 030802 (2019).
[42]H. Tang and Y. Li, "Design, analysis, and test of a novel 2-DOF nanopositioning system driven by dual mode," IEEE Trans. Rob. **29**, 650–662 (2013).
[43]M. Jia, R. P. Jia, and J. J. Yu, "A compliance-based parameterization approach for type synthesis of flexure mechanisms," J. Mech. Rob. **7**, 031014 (2015).
[44]H. J. Su, H. Shi, and J. Yu, "A symbolic formulation for analytical compliance analysis and synthesis of flexure mechanisms," J Mech. Des. **134**, 51009 (2012).
[45]S. Polit and J. Dong, "Development of a high-bandwidth XY nanopositioning stage for high-rate micro-/nanomanufacturing," IEEE/ASME Trans. Mechatron. **16**, 724–733 (2011).
[46]L. Howell, *Compliant Mechanisms* (China Higher Education Press, 2007).
[47]R. J. Roark, *Roark's Formulas for Stress and Strain* (McGraw-Hill, 2002).